Original research article

JSA

J Strain Analysis
1–17

DOI: 10.1177/03093247261447450
journals.sagepub.com/home/sdj
Sage

Shape optimization of spline-based punches for enhanced dry adhesion via a narrow neural network surrogate

Norbert Agócs[1] and Attila Kossa[1]

Abstract

The adhesion between a rigid substrate and spline-defined elastic punches is investigated with focus on the asymptotic normal stress near the contact edge. Interfacial stress distributions are obtained from automated finite element simulations in Abaqus using Python scripting. Based on these results, a surrogate-based optimization framework is developed in which a narrow feedforward neural network predicts the characteristics of the asymptotic normal stress solution from the punch geometry. The asymptotic normal stress solution allows for the semi-analytical determination of the energy release rate for edge-initiated interfacial defects, which is a primary governing factor of adhesion strength. The optimization aims to minimize the asymptotic normal stress. The results show that the proposed approach accurately captures the highly nonlinear geometry-stress relationship and identifies spline-based punch geometries with improved adhesion performance compared to a straight cylindrical punch. This framework can be used to design new geometries with improved adhesion characteristics. The data and code will be provided in the Supplemental Material for reproducibility and further exploration.

Keywords

asymptotic normal stress, dry adhesion, edge singularity, finite element analysis, neural network, surrogate modelling, shape optimization, spline-based geometry, deep learning

Date received: 6 January 2026; accepted: 2 April 2026

Introduction

Gecko-inspired fibrillar structures have been extensively investigated in recent years because of their potential applications in engineering areas including robotic handling and climbing, adhesion technologies and micro transfer printing.[1–8] The design and fabrication of these nano- and microfibrillar structures require a solid understanding of the mechanics that govern adhesion phenomena.[9] Among the many factors that affect adhesive performance, the stress distribution along the interface between the substrate and the fibrils is fundamental. Previous studies have shown that the geometry of the fibril profoundly influences the local stress state at the contact interface, which in turn determines the overall adhesion strength and stability.[10–13] Consequently, a primary objective in the design of fibrillar adhesive systems is to optimize the interfacial stress distribution by adjusting the geometry of the fibril.

A widely adopted strategy to reduce the magnitude of the normal stress component in the singularity domain is to modify the fibril tip geometry from a straight punch to a mushroom-shaped design.[14–18] This geometry redistributes the interfacial stresses, effectively reducing the concentration at the edge by altering the order of the singularity.[19] Both experimental and numerical studies have shown that this geometric modification can improve adhesion performance, particularly in cases where detachment initiates at the edge. Another approach to tuning the stress distribution involves using composite pillar structures with a soft tip and a stiff stalk.[20,21] The presence of a stiffer stalk can reduce the normal stress magnitudes near the edge singularity, while preserving the overall geometry of a

[1]Department of Applied Mechanics, Faculty of Mechanical Engineering, Budapest University of Technology and Economics, Budapest, Hungary

Corresponding author:
Attila Kossa, Department of Applied Mechanics, Faculty of Mechanical Engineering, Budapest University of Technology and Economics, Műegyetem RKP. 3, Budapest H-1111, Hungary.
Email: kossa@mm.bme.hu

straight punch. However, it should be noted that reducing the normal stresses near the edge singularity leads in both concepts to higher stresses toward the center of the punch, as the total normal force for a given applied load must remain constant to satisfy equilibrium. A further strategy to reduce the normal stresses in the singularity domain is the use of radially graded elastic modulus, which decreases toward the contact perimeter. Numerical investigations have demonstrated that such grading can significantly reduce the stress intensity near the edge, and for sufficiently strong gradients even eliminate the stress singularity altogether, leading to enhanced adhesion performance.[20,22]

Despite extensive research on the stress distributions in adhesive fibrillar systems, several challenges remain. Closed-form analytical solutions for the interfacial stress distribution have not been reported in the literature and are not expected to exist, even for the simplest straight cylindrical punch, due to its complexity. However, asymptotic approaches have been proposed to characterize the stress solution in the singularity.[23–27] The stress solution admits as a power-law representation in terms of the distance (ρ) from the perimeter. The stress distribution is governed by the leading, most singular term of this expansion, while higher-order terms become negligible. As a result, the asymptotic normal stress can be approximated by

$$\sigma_\infty(\rho) = C \cdot \overline{\sigma} \cdot \left(\frac{\rho}{D}\right)^{\beta}, \tag{1}$$

where ρ is the radial coordinate along the interface from the perimeter toward the center, D is the punch diameter, and $\overline{\sigma}$ is the average normal stress over the contact area, as indicited in Figure 1. The parameters C and β are geometry-dependent, dimensionless constants that characterize the intercept and slope of the asymptotic stress solution, respectively. The asymptotic stress expression in equation (1) can be rewritten in logarithmic form by substituting $D = 2a$, taking the base-10 logarithm of both sides, and rearranging the terms according to the standard properties of logarithms:

$$\begin{aligned} \log_{10}\left(\frac{\sigma_\infty}{\overline{\sigma}}\right) &= \log_{10}C - \beta\log_{10}\frac{1}{2} - \beta\log_{10}\left(\frac{\rho}{a}\right), \\ \log_{10}\left(\frac{\sigma_\infty}{\overline{\sigma}}\right) &= \alpha - \beta\log_{10}\left(\frac{\rho}{a}\right). \end{aligned} \tag{2}$$

Here, α is a dimensionless parameter that characterizes the asymptotic stress ratio at the center ($\rho = a$) of the punch. The relationship between the constant C and the α, β parameters is given by

$$\alpha = \log_{10}C - \beta\log_{10}\frac{1}{2} = \log_{10}C + 0.301\beta, \tag{3}$$

$$C = 10^{\alpha - 0.301\beta}. \tag{4}$$

The logarithmic representation of the asymptotic stress solution is useful for fitting numerical or experimental data in the singularity domain, as it enables a straightforward determination of the parameter α and β through linear regression in log–log space.

Note that the slope β of the asymptotic stress solution can be approximated analytically.[25] For a straight cylindrical punch, $\beta = -0.406$, while for other geometries β varies with the punch shape. Therefore, equation (2) can be used to describe the asymptotic stress characteristics in all cases.

To relate the interfacial stress distribution to adhesion strength, denoted by S, the detachment process is commonly analyzed by considering a small crack located in the singularity domain along the perimeter. The crack results in a singular stress solution at its tip, and the associated energy release rate can be evaluated using classical fracture mechanics. Thus, two different punch configurations can be compared based on their energy release rates to determine their adhesion strengths. This approach has been adopted in previous studies.[20,21] Here, the adhesion strength is inversely proportional to the parameter C:

$$S \propto \frac{1}{C}. \tag{5}$$

The smaller the parameter C the higher the adhesion strength. The asymptotic stress solution allows for the semi-analytical determination of the energy release rate associated with small interfacial defects near the contact perimeter.[25] By minimizing the dimensionless parameter C, the energy release rate for a given load is reduced, which directly enhances the resistance of the punch against edge-initiated detachment. Consequently, during the design of the punch geometries, we try to reduce the value of C in order to achieve stronger adhesion. The straight cylindrical punch serves as the reference configuration, for which $C_{\mathrm{SHP}} = 0.278$.[20] Note that the asymptotic stress solution primarily indicates the initiation of detachment, but does not fully characterize the complete separation process. Previous research has shown that detachment stability and the pull-off force involve complex crack propagation stages influenced by material and geometric constraints.[28,29] While these stability criteria are important, their investigation is outside the scope of this study.

Recent studies have increasingly employed deep learning to optimize the geometry of fibrillar adhesive structures, as no analytical solutions exist to directly relate geometry to interfacial stress distribution. Traditional simulations are limited by high computational cost, whereas data-driven approaches can efficiently capture the nonlinear relationships between fibril shape and interfacial stress response. Early applications of deep learning demonstrated that neural

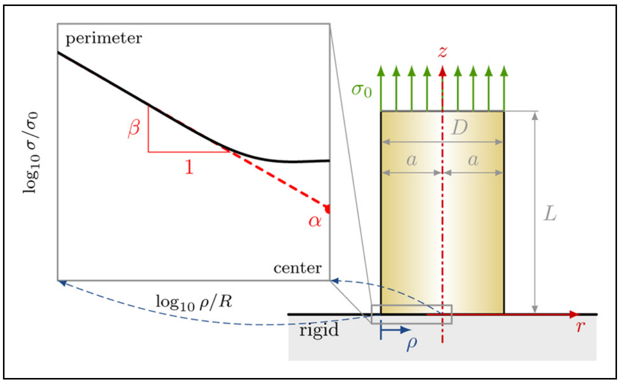

Figure 1. Schematic illustration of the straight cylindrical punch under uniform normal loading and the definition of the relevant geometric and stress-related quantities.

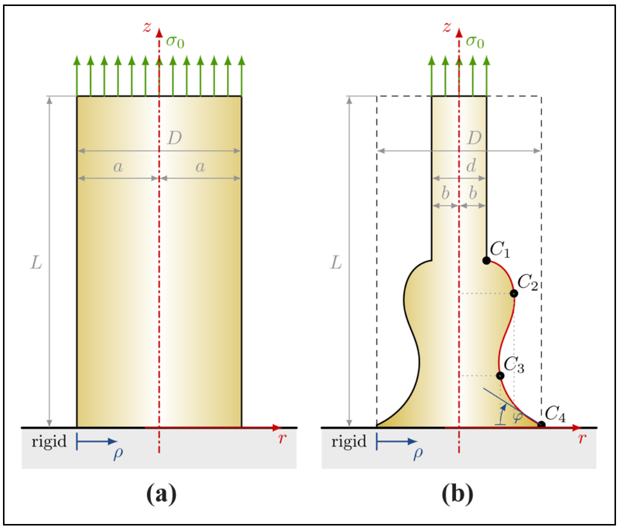

Figure 2. Geometry of the investigated punch models. Left: schematic of the straight cylindrical punch with diameter *D* and length *L*. Right: schematic of the arbitrary spline-based punch defined by the diameter *D*, stalk diameter *d*, and length *L*, with the spline-contour through the control points C_1–C_4.

networks could predict and optimize the shape of single-material adhesive pillars, revealing designs that suppressed edge singularities and improved pull-off strength.[30,31] Neural networks trained on finite element data have since been applied to predict and optimize fibril geometries, achieving nearly uniform stress fields and enhanced adhesion.[32–34] Other approaches have utilized deep neural networks as inverse design tools, capable of directly generating fibril geometries or compliance distributions that maximize adhesive performance while maintaining structural robustness.[35] More advanced implementations have adopted reinforcement learning, where an artificial agent iteratively modifies the fibril geometry based on feedback from finite element environments, autonomously discovering shapes with optimal concave-convex profiles and minimal interfacial stress gradients.[36]

In this study, a deep learning-based shape optimization framework is developed, with finite element simulations serving as the primary data source. Unlike previous approaches that rely on Bézier-based geometries, the proposed method employs spline-defined shapes characterized by a small number of control points. This representation is motivated by its integration in modern CAD and finite element environments, such as the sketch module of Abaqus, which supports direct implementation. The spline-based approach ensures the continuity of the contour while maintaining high flexibility for shape exploration. A key contribution of this work is the use of a narrow feedforward neural network—rather than neural networks with large numbers of parameters adopted in earlier studies—trained on the asymptotic stress distribution in the vicinity of the contact edge. The optimization objective is to enhance the adhesion strength under normal loading conditions using the asymptotic solution, while interfacial sliding and material defects are neglected. The mechanical model of the adhesive punch is introduced in *Mechanical model*. The finite element simulations, the dataset preparation, the neural network surrogate model, and the optimization approach are detailed in *Methods*. *Results and discussion* presents the optimization results and compares the optimized spline-based punches with the reference straight cylindrical punch. Finally, *Conclusions* summarizes the main findings and outlines directions for future work. The appendices provide Supplemental Information and further support the main findings of the study.

Mechanical model

The investigated problem is depicted in Figure 2. Two types of punches are considered: a straight cylindrical punch with diameter D and length L, which serves as the reference configuration, and a spline-based punch with used for shape optimization studies. The spline-based punch is defined by the diameter D, the stalk diameter d, and the length L, while its contour is generated by a spline fitted through the control points C_1-C_4. The number of control points is selected based on preliminary simulations. Four control points provides sufficient flexibility to explore a wide range of shapes.

Both punches are attached ideally to a flat rigid substrate. The loading consists of a vertical tensile force F applied to the punch's free end, yielding a uniform tensile stress σ_0. The axisymmetric section is described in polar coordinates r and z. The material of the punch is considered linear elastic, characterized by a homogeneous elastic modulus E and Poisson's ratio ν. The geometric, material, and loading parameters of the punch are summarized in Table 1. Note that the punch radius is defined as $a = \frac{D}{2}$ and the stalk radius as $b = \frac{d}{2}$. The punch material is represented by polydimethylsiloxane (PDMS) with the given elastic properties.[37,38] However, the specific value of the elastic modulus E does not affect the form of the stress solution, but only scales

Table 1. Geometric, material and load parameters of the punch.

Parameter	Symbol	Value
Punch diameter	D	2 mm
Stalk diameter	d	1.4 mm
Punch length	L	5 mm
Young's modulus	E	1 MPa
Poisson's ratio	ν	0.495
Applied tensile stress	σ_0	1 MPa

the stress magnitude, which is not relevant when comparing different geometries to the straight punch.

The non-zero stress components in the cylindrical coordinate system are σ_r, σ_θ, σ_z, and τ_{rz}, resulting in the following stress tensor:

$$\boldsymbol{\sigma} = \begin{bmatrix} \sigma_r & 0 & \tau_{rz} \\ 0 & \sigma_\theta & 0 \\ \tau_{rz} & 0 & \sigma_z \end{bmatrix}. \tag{6}$$

Our analysis focuses exclusively on the normal stress component σ_z acting perpendicular to the interface, as it is the primary driver of edge-initiated detachment in dry adhesion. For the sake of briefness, this component is denoted simply by σ, and the term *asymptotic stress* refers specifically to this asymptotic normal stress component σ_z throughout the remainder of this paper. Our objective is to evaluate the distribution of the σ stress component along the interface. Due to the complexity of the problem, no closed-form analytical stress solutions are available. Therefore, the stress solutions are determined numerically using the finite element method.

The analysis is performed within the framework of the small-strain formulation under quasi-static conditions, assuming purely normal loading. The punch material is treated as linear elastic, as PDMS behaves nearly linear-elastically in the relevant deformation range, and detachment typically occurs before the material reaches the nonlinear elastic region.[39] Furthermore, the interface is modeled with a perfect bonding condition, meaning that partial slip, sliding, or separation during the loading process are not considered. While these assumptions simplify the complexity of real adhesive systems, they allow for a focused investigation on how geometry alone influences the initial stress distribution and the resulting adhesion strength.

Methods

The methodology of this study follows a structured four-step procedure, as illustrated in Figure 3. The process initiates with automated finite element models are generated, executed, and post-processed in Abaqus using Python scripting.[40–42] Subsequently, a dataset is assembled that links punch geometries to their corresponding asymptotic interfacial stress distributions. This dataset enables the training of a neural network acting as a surrogate model, which predicts the asymptotic normal stress solution based on the punch geometry. In the final stage, the neural network is embedded into an optimization framework to identify the optimal punch profiles that minimizes the asymptotic normal stress σ_∞ at the interface (see Figure 1). The following subsections describe the finite element workflow, dataset preparation, neural network model, and optimization procedure in detail.

Finite element simulation

The finite element simulations are performed in the commercial FEA software Abaqus with Python scripting for automation.[43] The punches are modeled as a two-dimensional axisymmetric problem with the geometric dimensions D, d, and L summarized in Table 1. The punch contour is defined by a cubic spline curve interpolated through four control points $C_1 \ldots C_4$, implemented using the available Sketch toolbox in Abaqus. The coordinates of the control points are expressed in the polar coordinate system (r, z). While C_1 and C_4 are fixed, the positions of C_2 and C_3 are variable within an admissible design domain. The control point C_4 is placed at the contact interface at the punch perimeter, whereas C_1 is located at the stalk perimeter at half the punch length (Figure 2), since the upper half of the punch has a negligible effect on the interfacial stress distribution for $L/a \geqslant 4$.[20] In all simulations, the fixed control points are assigned the following coordinates:

$$\begin{aligned} C_{1r} = b, C_{1z} = \frac{L}{2}, \\ C_{4r} = a, C_{4z} = 0, \end{aligned} \tag{7}$$

while the remaining control point coordinates C_{2r}, C_{2z}, C_{3r}, and C_{3z} are the design variables selected within the admissible design domain $\mathcal{C}$. The admissible design domain $\mathcal{C}$ is defined by geometric bounds that ensure the resulting spline contours remain well-defined, do not have self-intersections, and stay within the overall punch geometry. In particular, the design variables are constrained as follows:

$$\mathcal{C} = \begin{cases} C_{2r} \in [0.5ba], & C_{3r} \in [0.75ba], \\ C_{2z} \in [0.25L0.35L], & C_{3z} \in [0.1L0.2L] \end{cases}. \tag{8}$$

Simulations are performed for a wide range of punch geometries by systematically varying the positions of the control points C_2 and C_3 within the domain $\mathcal{C}$. The punch shape is varied only over its lower as the geometric influence of the upper stalk

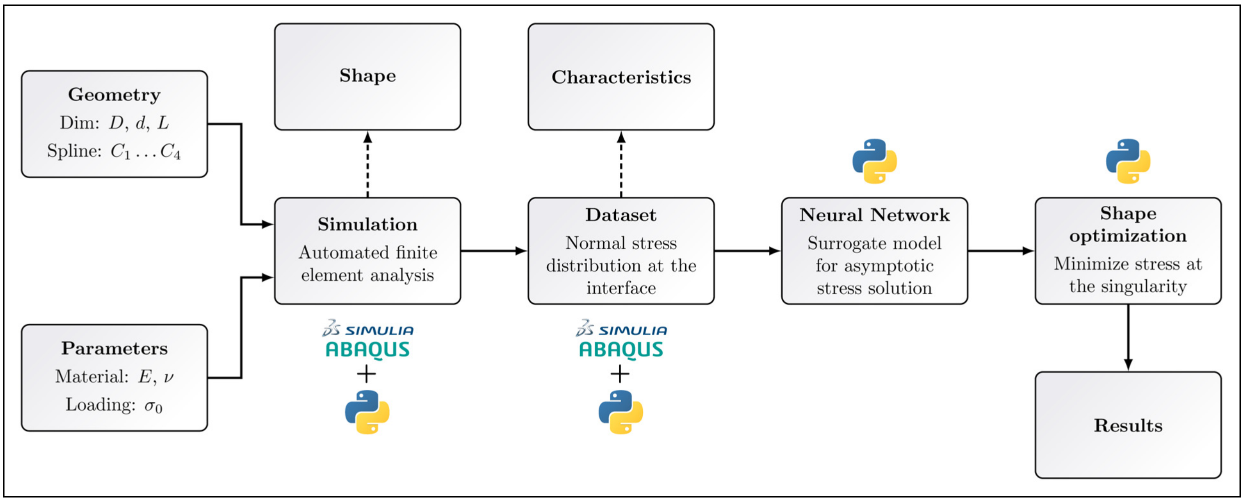

Figure 3. Schematic illustration of the overall workflow for the shape optimization framework of spline-based punches.

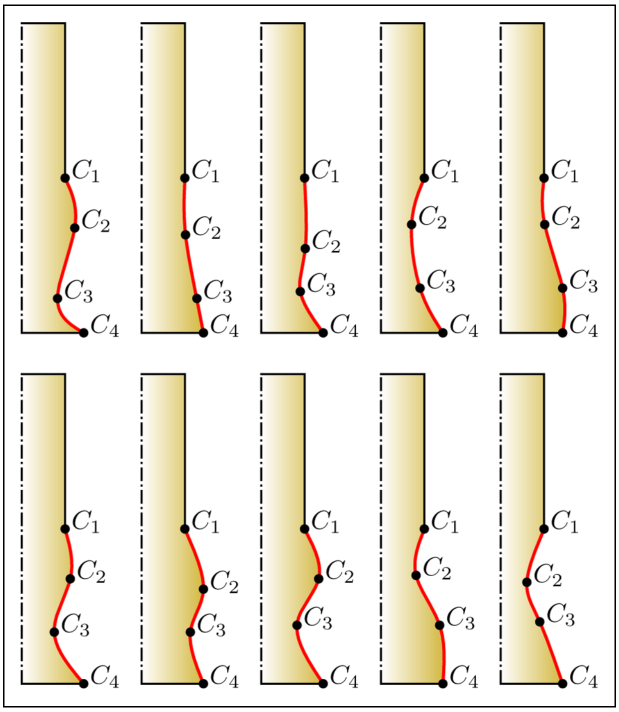

Figure 4. Examples of the shapes generated by varying the control points C_2 and C_3 within the admissible design domain. The fixed control points C_1 and C_4 are also shown.

region on the singularity is negligible. A grid-based sampling of the domain yields a total of 10,000 distinct punch configurations. Several examples are shown in Figure 4 with the coordinates listed in Table 2 for illustration purposes.

The axisymmetric section of the punch models is discretized using four-node bilinear axisymmetric quadrilateral elements with hybrid formulation (CAX4H) and full termed Gaussian integration. Each simulation employs approximately 100,000–120,000 elements. To resolve the sharp stress gradients near the contact edge, mesh refinement is applied in the vicinity of the interface and within the singularity domain to accurately capture the stress distribution. The adequacy of the discretization was confirmed via a mesh convergence study. An example of the finite element mesh for a spline-based punch is illustrated in Figure 5. The punch is fixed at its bottom edge to model adhesion to the rigid substrate, while the top edge is loaded uniformly with the tensile stress σ_0 and no shear traction. The stress results are normalized by the applied tensile stress σ_0.

For each configuration, the finite element simulation is carried out to determine the normal stress distribution σ along the interface. Note that although the other stress components are also available from the simulations, the normal stress in the z-direction has the most significant influence on adhesion strength.[26]

Dataset preparation

The present work aims to quantify the relationship between the punch geometry and the resulting asymptotic stress distribution at the interface. This is achieved by constructing a dataset that couples specific punch configurations with their respective asymptotic stress characteristics derived from automated finite element simulations. The punch geometry is parameterized using the design variables corresponding to the control points C_2 and C_3, as defined in equation (7), together with the calculated angle φ of the spline's tangent at C_4. While φ is geometrically dependent on the control point positions, its inclusion as an explicit input feature provides the surrogate model with direct information regarding the local contact edge geometry, thereby enhancing the learning process. Let $\mathbf{c} = (C_{2r}, C_{2z}, C_{3r}, C_{3z}) \in \mathcal{C}$ denote the vector of design variables within the admissible design domain $\mathcal{C}$. The resulting dataset is:

$$\{(\mathbf{c}_i, \varphi_i, \alpha_i, \beta_i)\}_{i=1}^{N}, \tag{9}$$

Table 2. The numerical coordinates of all control points C_1–C_4 associated with each configuration reported in Figure 4.

#	C_{2r}/a	C_{2z}/L	C_{3r}/a	C_{3z}/L
1	0.856	0.339	0.578	0.111
2	0.711	0.317	0.894	0.111
3	0.711	0.272	0.631	0.133
4	0.494	0.350	0.631	0.144
5	0.711	0.350	1.000	0.144
6	0.783	0.339	0.525	0.167
7	1.000	0.306	0.789	0.167
8	0.928	0.339	0.578	0.189
9	0.422	0.328	0.631	0.200

The coordinates are normalized with respect to the punch radius a and length L, respectively.

where N is the total number of simulated punch configurations, φ_i is the tangent angle at C_4, and α_i and β_i are the regression parameters characterizing the asymptotic normal stress distribution for the i-th configuration.

The normal stress distributions are nearly linear in the log–log domain over the interval $\rho/a \leqslant 10^{-2}$, which enables a linear regression of the corresponding asymptotic stress parameters.[25] The radial coordinate is defined as $\rho/a = 1 - r/a$, measuring the inward distance from the punch perimeter toward its center, as shown in Figure 2. This linear regime allows for a determination of the asymptotic stress solution α and β by performing a linear regression to the interfacial stress distribution in the log–log domain (see Figure 1). Within this framework, both the slope β and the intercept α of the logarithmic relation are identified directly from the numerical data. The parameters are computed using the Ordinary Least Squares (OLS) method[44] applied to the finite element results, based on the logarithmic form of the asymptotic stress expression given in equation (2). The regression problem is written as

$$\begin{bmatrix} \alpha \\ \beta \end{bmatrix} = (\mathbf{X}^T\mathbf{X})^{-1}\mathbf{X}^T\mathbf{y},$$
$$\mathbf{X} = \begin{bmatrix} 1 & x_1 \\ 1 & x_2 \\ \vdots & \vdots \\ 1 & x_N \end{bmatrix}, \mathbf{y} = \begin{bmatrix} y_1 \\ y_2 \\ \vdots \\ y_N \end{bmatrix}, \tag{10}$$

where $x_i = \log_{10}(\rho_i/a)$ and $y_i = \log_{10}(\sigma_i/\overline{\sigma})$ for $i = 1, 2, \ldots, N$ denote the numerical data points at the interface.

The final dataset comprises $N = 9589$ samples, each containing the design variables $\mathbf{c}_i$, the tangent angle φ_i, and the corresponding asymptotic stress parameters α_i and β_i. This final sample count is slightly lower than the total number of initially generated configurations, as cases where the automated finite element simulations failed to converge were excluded. The cleaned dataset is stored in a structured CSV format for easy loading and processing. In addition, all finite element simulation results—including filename, design variables (all control points and spline's tangent angle), normal stress solution, and the calculated asymptotic stress solutions—are archived in JSON format to ensure reproducibility. See Appendix 1 for more details regarding the dataset structure.

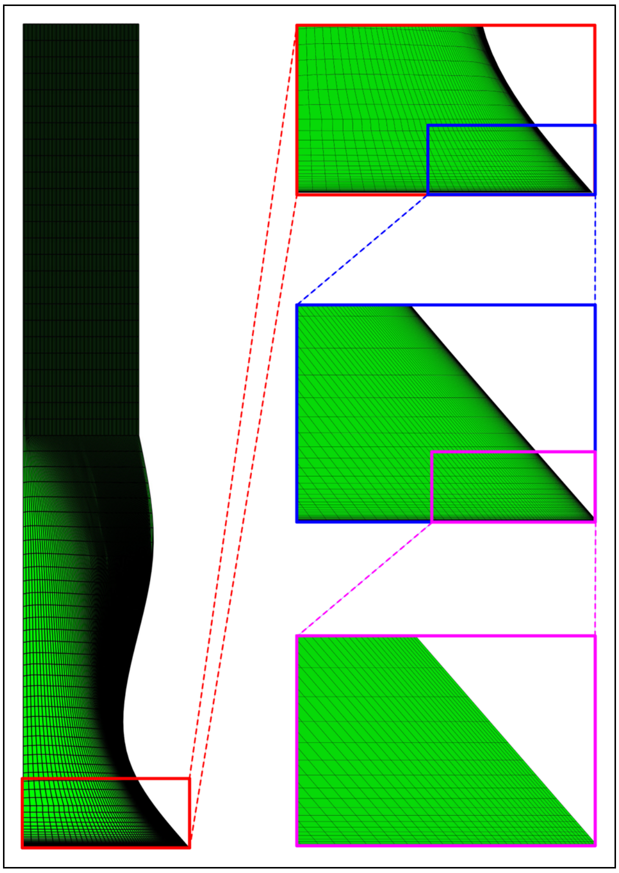

Figure 5. Finite element mesh of a spline-based punch.

Neural network model

A narrow feedforward neural network is developed to learn the mapping between the punch geometry and the corresponding asymptotic normal stress solution.[44–46] A narrow neural network refers to a network architecture with a small number of neurons per hidden layer, resulting in a limited number of trainable parameters while retaining sufficient depth to capture the nonlinearity of the mapping. The choice of a narrow architecture is motivated by the desire to reduce the number of trainable parameters aiming to achieve high predictive accuracy with minimal complexity, in contrast to the deep neural networks with large parameter counts commonly used in previous studies.[30,32,36]

The applied narrow network architecture, as shown in Figure 6, consists of an input layer, q hidden layers

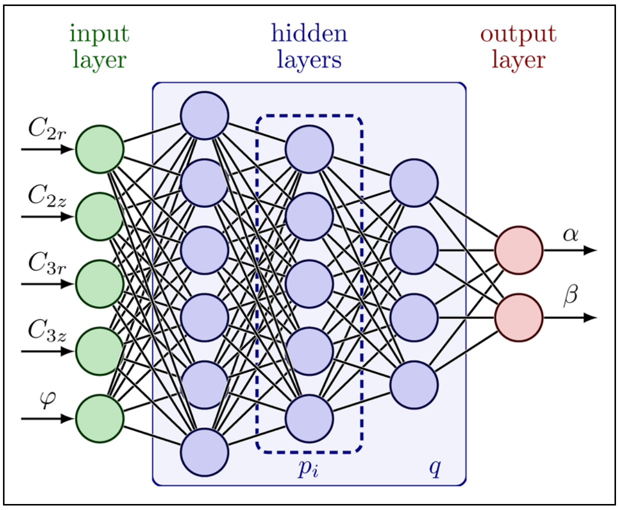

Figure 6. Schematic illustration of the narrow feedforward neural network (FNN) mapping the input vector $(C_{2r}, C_{2z}, C_{3r}, C_{3z}, \varphi)$ to the asymptotic stress parameters (α, β) using q hidden layers with p_i neurons each.

with p_i neurons each and ReLU activation functions, and an output layer with a linear activation function.

The input layer receives the five-dimensional vector comprising the design variables $\mathbf{c}$ and the tangent angle φ. By explicitly including φ as an input, the network is relieved from the task of internalizing this nonlinear geometric relationship, which significantly streamlines the training process. The output layer produces the two-dimensional vector containing the asymptotic stress parameters α and β. The mapping established by the neural network can be expressed mathematically as

$$\mathcal{N} : \mathbb{R}^5 \rightarrow \mathbb{R}^2 \mathcal{N}(\mathbf{c}, \varphi) = (\alpha, \beta), \tag{11}$$

where $\mathcal{N}$ denotes the neural network operator.[47] The neural network is implemented in Python using the open-source Keras library.[40]

The dataset is partitioned into training (80%), validation (10%), and test (10%) subsets. To ensure numerical stability and accelerate convergence, all input features are standardized to have zero mean and unit variance. Note that the output targets are not standardized. Such a training-validation-test split, together with input feature standardization, follows standard practice in supervised learning to ensure reliable training.[48,49] The neural network is trained using the Adam optimizer with a mean squared error (MSE) loss function.[44,45,49] Training is performed for up to 500 epochs with a batch size of 64, and early stopping based on the validation loss is employed to prevent overfitting.[50,51] The learning rate is set to 10^{-3}. These hyperparameters are determined empirically through preliminary numerical experiments, as no universally optimal or closed-form choices exist for these settings. Hyperparameter optimization is carried out via a grid search over the number of hidden layers q and the number of neurons p_i in each layer. The best-performing configurations are summarized in Table 3 and their training and validation loss curves are shown in Figure 7.

Table 3. Best-performing neural networks obtained through hyperparameter tuning, including the total number of trainable parameters (n_{par}), the number of training epochs (n_{ep}), and the corresponding test set performance metrics. RMSE, and MAE denoting the root mean squared error, and mean absolute error, respectively.

$q \mid (p_i)$	n_{par}	n_{ep}	$RMSE_{test}$	MAE_{test}
$3 \mid (11, 11, 5)$	270	500	0.0027	0.0019
$3 \mid (11, 10, 6)$	266	270	0.0029	0.0021
$3 \mid (12, 8, 8)$	266	398	0.0031	0.0022
$3 \mid (12, 12, 7)$	335	228	0.0031	0.0023
$3 \mid (11, 11, 7)$	298	248	0.0033	0.0025
$3 \mid (12, 8, 3)$	211	307	0.0036	0.0027
$3 \mid (9, 10, 6)$	234	237	0.0038	0.0028
$3 \mid (12, 6, 7)$	215	279	0.0039	0.0029

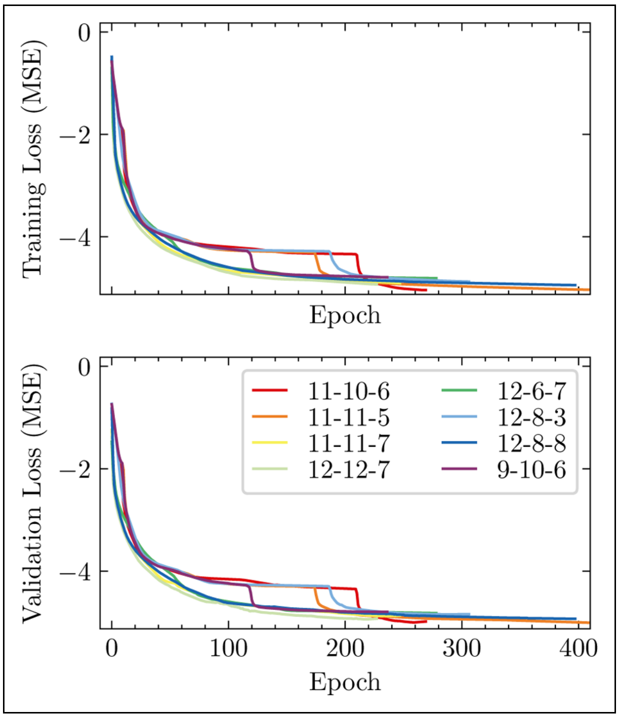

Figure 7. Training (top) and validation (bottom) loss curves (MSE) for the best-performing FNNs obtained from the hyperparameter tuning, plotted on a $\log_{10}$ scale along the vertical axis.
The results demonstrate stable convergence across architectures, with early stopping terminating training once the validation loss ceases to improve.

The final model architecture is selected according to the lowest MSE achieved on the test set. Accordingly, the selected architecture consists of $q = 3$ hidden layers with $p_i = (11, 11, 5)$ neurons, respectively. This model is subsequently employed as a surrogate model for carrying out the shape optimization procedure.

Shape optimization

The adhesion performance of the punch is primarily governed by the interfacial normal stress distribution, in particular by the stress singularity developing near the punch edge.[10,20,21] Note that the calculations are performed only for cases having a stress singularity, which depends on the tangent angle φ. From a fracture mechanics perspective, adhesion failure is treated as the initiation of a small interfacial crack within the singularity zone. The adhesion strength scales inversely proportional with the dimensionless parameter C as shown in equation (5). Consequently, for configurations with identical material properties, a reduction of the parameter C leads to an increase in the attainable adhesion strength. The straight punch ($C_{\mathrm{STP}} = 0.278$) provides a reference benchmark to quantify the performance gain achieved through shape optimization. Based on this relation, the objective of the shape optimization is to minimize the value of the dimensionless parameter C, thereby maximizing the adhesion strength of the punch. Using the trained neural network as a surrogate model, the optimization problem is formulated as:

$$\mathbf{c}^* = \arg\min_{\mathbf{c}\in\mathcal{C}} C(\alpha, \beta) = \arg\min_{\mathbf{c}\in\mathcal{C}} C(\mathcal{N}(\mathbf{c}, \varphi)), \quad (12)$$

where $\mathbf{c}^*$ denotes the optimal design variable vector and $\mathcal{N}(\mathbf{c}, \varphi)$ represents the neural network prediction of the asymptotic stress parameters for a given punch geometry defined by $\mathbf{c}$ and φ. The use of the surrogate model reduces the computational cost associated with objective function evaluations, compared to direct finite element simulations achieving a speed-up on the order of 10^5, thereby enabling an efficient exploration of the design space.

For numerical convenience, the optimization is carried out using an equivalent objective function derived from the dimensionless parameter C. Given that $C = 10^{\alpha - 0.301\beta}$, minimizing C is equivalent to minimizing the exponent

$$Q(\mathbf{c}) = \alpha(\mathbf{c}, \varphi) - 0.301\beta(\mathbf{c}, \varphi), \quad (13)$$

which is monotonically related to original expression. Accordingly, the optimal punch geometry is obtained by minimizing $Q(\mathbf{c})$ over the admissible design domain $\mathcal{C}$. Note that the tangent angle φ is not independent but is computed directly from the design variables $\mathbf{c}$. The resulting optimal design $\mathbf{c}^*$ corresponds to the punch geometry with the lowest predicted C, and thus the highest attainable adhesion strength within the considered design space.

The optimization problem is solved using the Differential Evolution (DE) algorithm,[52] a global, population-based optimization strategy. The DE is particularly well suited for the present application, as the surrogate-based objective function is generally nonconvex and may exhibit multiple local minima. DE operates on a population of candidate solutions and iteratively improves them through mutation, crossover, and selection, allowing for exploration of the design space and identification of near-global optima. The optimization is performed with respect to the design variable vector $\mathbf{c}$. The fitness function minimized by the DE algorithm is given by $Q(\mathbf{c})$. The population size is chosen proportional to the number of design variables, and the optimization is initialized with random candidate solutions within the $\mathcal{C}$ domain. The algorithm is executed for a fixed maximum number of generations or until convergence is reached. Convergence is reached when no further improvement in the objective function is observed, as shown in Figure 8.

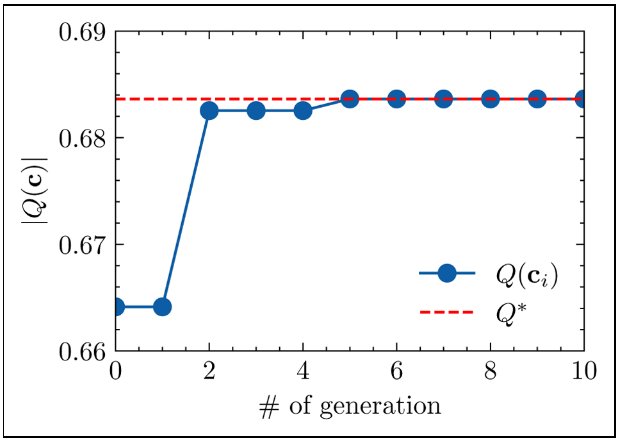

Figure 8. Convergence of the objective function $Q(\mathbf{c})$ during the differential evolution optimization.
The dashed line denotes the optimal value Q^*.

Note that the DE algorithm was implemented using the SciPy library, which relies on well-established internal parameters to ensure reliable convergence.[53] While specific alternative algorithms might offer faster convergence in certain cases, the DE method was selected for its known robustness in navigating complex, nonconvex design spaces.

Results and discussion

Results of finite element simulations and dataset preparation

The results of the finite element simulations provide the normal stress distributions along the interface for all investigated punch configurations. The asymptotic stress parameters α and β are extracted from these distributions through linear regression in the log–log domain. The quality of the regressions is characterized using the coefficient of determination, R^2. The average R^2 value across all fits is 0.9996, demonstrating a high degree of correlation between the models and the measured data. Based on this, the asymptotic stress solutions can be considered reliable. Examples of the normal stress distributions along with the fitted asymptotic stress solutions are illustrated in Figure 9, along

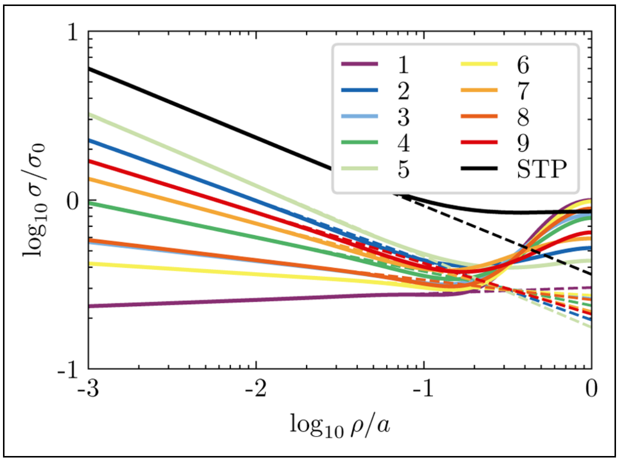

Figure 9. The normal stress distributions $\log_{10}(\sigma/\sigma_0)$ as a function of the normalized radial coordinate $\log_{10}(\rho/a)$ for the selected spline-based punch configurations.
Solid lines denote the finite element solutions, while dashed lines indicate the corresponding asymptotic fits. The reference solution for the cylindrical straight punch (STP) is shown for comparison.

Table 4. Numerical parameters of the asymptotic stress solutions (α, β) and the corresponding coefficients of determination (R^2) for the representative spline-based punch configurations shown in Figure 9.

#	φ [°]	α [1]	β [1]	R^2
1	30.6	−0.5180	0.0368	0.9996
2	80.2	−0.7105	−0.3545	0.9998
3	54.3	−0.5833	−0.1113	0.9997
4	56.7	−0.6250	−0.2022	0.9998
5	81.3	−0.7543	−0.4205	0.9998
6	49.9	−0.5644	−0.0627	0.9997
7	68.1	−0.6604	−0.2616	0.9998
8	56.3	−0.5903	−0.1175	0.9997
9	71.1	−0.6762	−0.3021	0.9998

with the corresponding numerical parameters listed in the accompanying Table 4. Additionally, the influence of the Poisson's ratio was evaluated within the nearly incompressible range. As detailed in Appendix 2, the stress solutions have negligible sensitivity to this parameter, with a mean relative difference of only 0.42%.

The calculated values of β, which represent the slope of the asymptotic stress solution, indicate that the punch geometry significantly influences the stress singularity order at the contact perimeter. As illustrated in Figure 9, the change in the slope of the stress solutions clearly demonstrates the modification of the singularity's nature. Specifically, varying the tangent angle φ leads to a shift in β, suggesting that the edge geometry can alter the characteristics of stress solutions. This is consistent with findings for mushroom-like geometries,[19] where the edge angle θ determines whether the stress remains finite or a singularity is present. In certain configurations, the stress solutions tend toward mitigating or eliminating the singularity depending on the local tangent, although a more comprehensive analysis of this phenomenon remains beyond the scope of the present work.

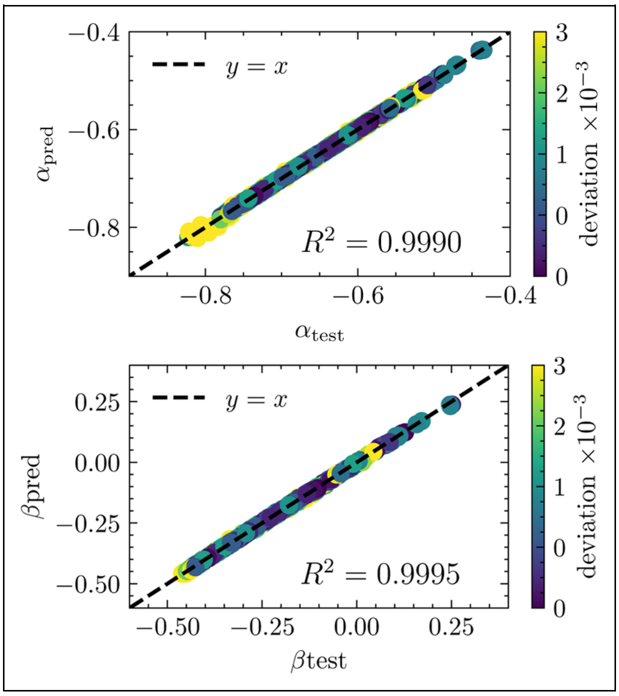

Figure 10. Parity plots comparing the predicted and reference values of the asymptotic stress parameters: (top) α and (bottom) β evaluated on the test dataset.
The dashed line indicates the ideal parity relation $y = x$. The color of the markers represents the absolute deviation from the parity line, defined as the perpendicular distance from $y = x$.

Predictive capability of the neural network

The predictive performance of the neural network on the test dataset is evaluated using parity plots that compare the predicted and reference values of the asymptotic stress parameters, as shown in Figure 10.[44,45] For both parameters, α and β, the predictions correlate closely with the corresponding reference values, as indicated by the clustering of the data points around the ideal parity line $y = x$. This correlation is quantitatively supported by high coefficients of determination, with $R^2 = 0.9990$ for α and $R^2 = 0.9995$ for β. No systematic bias is observed over the investigated parameter range, and deviations from the parity line remain small even for extreme values of the parameters. The color-coded absolute deviation from the parity line further confirms that larger errors are sparse and do not accumulate in specific regions of the parameter space. Overall, these results demonstrate that the trained neural network captures the nonlinear relationship between the punch geometry and the asymptotic stress parameters.

The asymptotic normal stress distributions reconstructed from the neural network predictions are

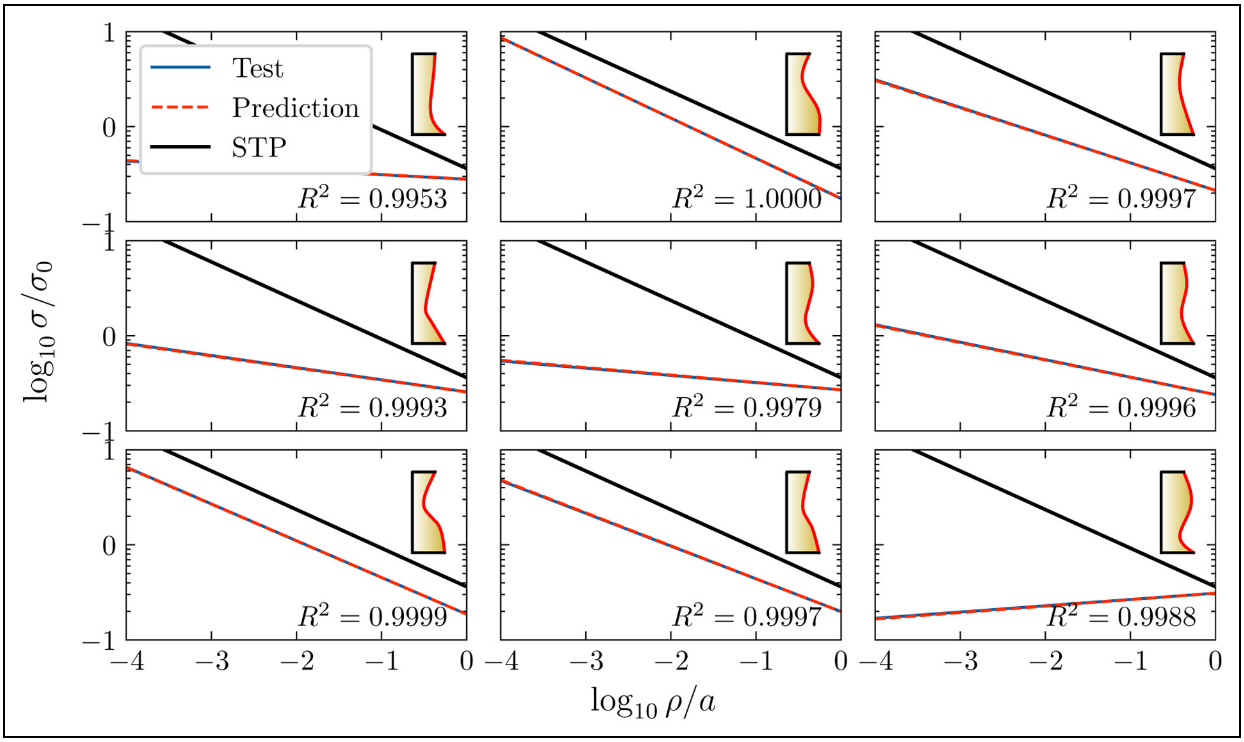

Figure 11. Comparison of the predicted and reference asymptotic normal stress distributions for representative test samples. Blue solid lines denote the finite element results, red dashed lines the FNN predictions, the black solid line the straight punch (STP) reference. The corresponding spline-punch geometries are also shown.

compared with the corresponding finite element results for representative test samples in Figure 11. The straight punch (STP) response is included as a benchmark for reference.

The neural network accurately captures the characteristic asymptotic behavior of the normal stress solution and provides predicted stress curves consistent with the finite element results over the entire range of the normalized radial coordinate ρ/a. Notably, this agreement remains robust in the vicinity of the punch edge ($\rho \to 0$), where the stress singularity dominates the adhesion behavior. These results demonstrate that the surrogate model preserves the physically relevant features of the asymptotic stress field.

The statistical characteristics of the prediction errors are further examined by evaluating the mean relative error for each test sample, defined as

$$\bar{\varepsilon}_{\mathrm{rel}} = \frac{1}{N}\sum_{j=1}^{N}\left|\frac{\sigma_\infty^{\mathrm{FNN}}(\rho_j) - \sigma_\infty^{\mathrm{FEA}}(\rho_j)}{\sigma_\infty^{\mathrm{FEA}}(\rho_j)}\right|, \tag{14}$$

where $\sigma_\infty^{\mathrm{FNN}}(\rho_j)$ and $\sigma_\infty^{\mathrm{FEA}}(\rho_j)$ denote the neural network prediction and the corresponding finite element reference value of the asymptotic normal stress at the j-th radial coordinate ρ_j, respectively, and N is the total number of evaluation points along the interface. The distribution of the mean relative error $\bar{\varepsilon}_{\mathrm{rel}}$ across the test dataset is shown in Figure 12 and provides a comprehensive measure of the accuracy and reliability of the surrogate model. The relative error values range from 0.01% to 2.89%, with a mean of 0.365% and a standard deviation of 0.31%. The median relative error is 0.298%.

Overall, the neural network surrogate model demonstrates strong generalization capability for previously unseen punch geometries within the admissible design domain. The model reliably maps the geometric design variables to the asymptotic stress parameters, enabling accurate reconstruction of the interfacial asymptotic normal stress distributions.

Optimized spline-based punch geometry

The shape optimization based on the trained neural network surrogate model leads to a significant reduction of the dimensionless parameter C compared to the straight punch (STP) reference. For the straight punch, the benchmark value is $C_{\mathrm{STP}} = 0.278$, whereas the best-performing optimized spline-based punch achieves a minimum value of $C_{\min} \approx 0.207$. This corresponds to an absolute reduction of $\Delta C = 0.071$, which represents a relative decrease of approximately 25.5% with respect to the straight punch. Since the adhesion strength scales inversely with C, this reduction directly translates into a substantial improvement in the attainable adhesion performance. Note that the identified optimal parameters, while positioned at varying distances from the center of the admissible design domain $\mathcal{C}$, remain distinct interior points. Specifically, the variables r_3 and z_3

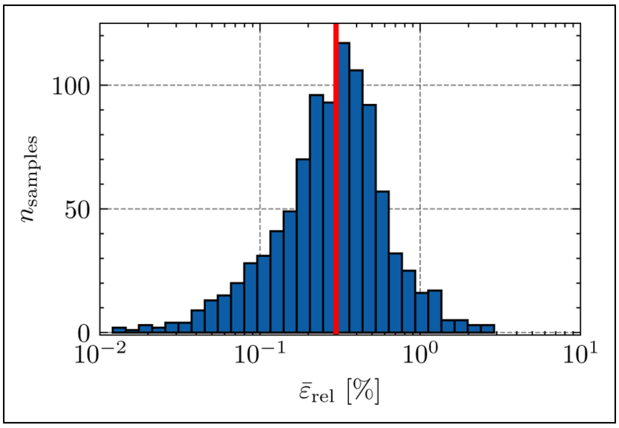

Figure 12. Distribution of the mean relative prediction error $\bar{\varepsilon}_{\mathrm{rel}}$ over the test dataset.
The red vertical line indicates the median error value.

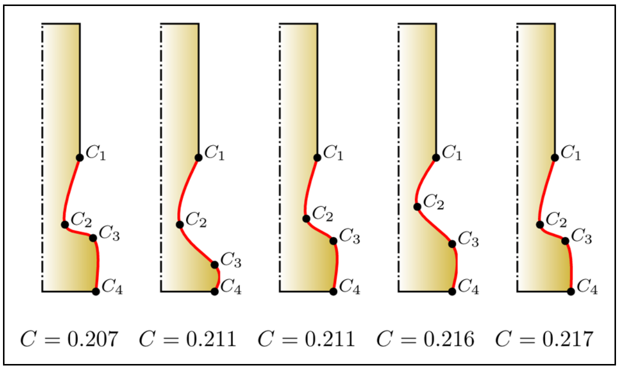

Figure 13. Best-performing optimized spline-based punch geometries ranked by the dimensionless parameter C.
The spline control points C_1–C_4 and the corresponding C values are indicated for each configuration.

converge to values representing approximately 96% of their respective allowed ranges, approaching the upper boundaries. Conversely, r_2 and z_2 are in the lower portion of the design space, at approximately 5% and 26% of their permitted intervals, respectively. This confirms that the optimization identified a numerical minimum within the prescribed bounds, and the optimization process was not truncated by the geometric constraints.

The geometries corresponding to the best-performing optimized designs are shown in Figure 13.

As the value of C decreases, a geometric trend can be observed: the optimized spline-based punch shapes increasingly resemble the characteristic profile of a mushroom punch. However, due to the imposed admissible design domain, the optimization process cannot fully recover the classical mushroom punch geometry. Instead, the algorithm converges to spline-based shapes that represent the closest admissible approximation of the optimal shape within the prescribed design space.

The corresponding asymptotic normal stress distributions of the optimized spline-based punches are presented in Figure 14, together with their associated

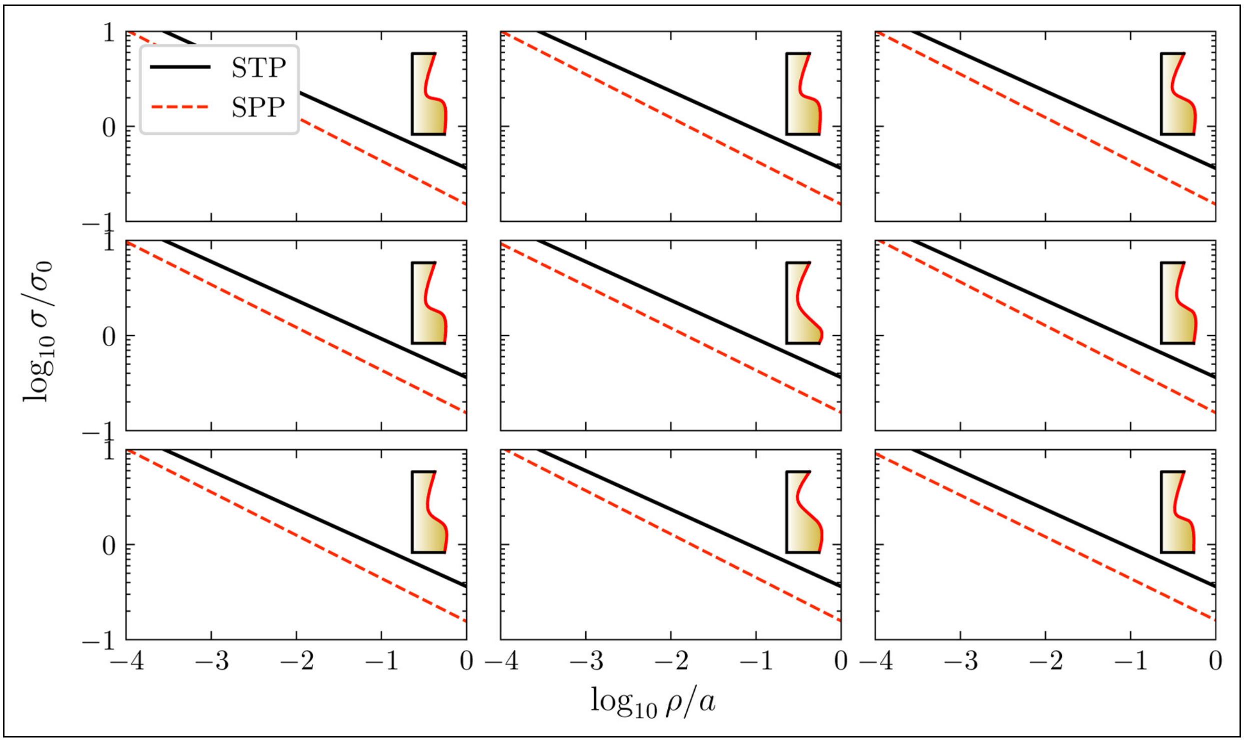

Figure 14. Asymptotic normal stress distributions for the optimized spline-based punch geometries (SPP, red dashed line), shown in comparison with the straight punch (STP, black solid line) references.
The corresponding punch geometries are also displayed.

Table 5. Computational time comparison between the finite element analysis (FEA) and the neural network (NN) for different numbers of samples (*n*).

n	FEA time	NN time
1	15 s	4.97×10^{-5} s
10	150 s (2.5 min)	4.97×10^{-4} s
100	1,500 s (25 min)	4.97×10^{-3} s
1000	15,000 s (≈4.17 h)	0.0497 s
10,000	150,000 s (≈41.67 h)	0.497 s

geometries. For reference, the asymptotic stress distributions of both the straight punch (STP) is also included.

The figure clearly demonstrates that the optimized spline-based punch geometries achieve a noticeable reduction of the asymptotic normal stress level compared to the straight punch over the entire range of the normalized radial coordinate. In particular, the stress singularity near the punch edge is mitigated relative to the straight punch case, which explains the observed decrease in the parameter *C*. The comparison with the straight punch reveals that, the optimized spline-based punches significantly outperform the straight punch. Overall, the results demonstrate that the proposed surrogate-based optimization framework successfully identifies geometries with improved adhesion characteristics. The accuracy of the framework for the best-performing geometries is further confirmed by finite element validation in Appendix 3.

Efficiency of the surrogate model compared to finite element analysis

The trained neural network surrogate model offers a significant computational advantage over the traditional finite element analysis. While a single high-resolution finite element simulation—including automated meshing and post-processing—requires approximately 15 s, the neural network provides the same prediction in 4.97×10^{-5} s. This represents a speed-up factor of more than 3×10^{5}.

The performance gain is further illustrated by evaluating large datasets, as summarized in Table 5. For a batch of 10000 evaluations, which is typical for global optimization tasks, the direct finite element analysis would need over 41 h of continuous computation. In contrast, the neural network completes the same task in less than 0.5 s. Notably, by replacing the computationally expensive finite element analysis with this near-instantaneous surrogate model, the optimization process allows for a more extensive exploration of the spline-based design space.

Modeling assumptions and limitations

The surrogate-based optimization framework presented in this study is built upon the modeling assumptions and simplifications detailed in Section. The material is treated as linear elastic, and the interface is modeled under quasi-static, normal loading with perfect bonding conditions.

The present study adopts a simplified mechanical description with linear elastic material behavior and purely normal loading. Such assumptions are commonly used in the analysis of fibrillar adhesive contacts and allow the influence of geometry on the interfacial stress distribution to be examined in a clear manner. Viscoelastic effects may become relevant in dynamic or rate-dependent adhesion processes. However, previous studies on fibrillar structures have shown that, under quasi-static conditions or in defect-free contacts, the pull-off response can often be well approximated by an elastic framework.[54,55] Extensions toward viscoelastic material models could therefore be considered in future work when explicitly addressing dynamic detachment phenomena.

In the present model the interface is assumed to remain perfectly bonded, that is, slip is not considered. Partial slip could be incorporated through appropriate interfacial contact or cohesive laws; however, significant sliding is typically accompanied by geometric nonlinearity and larger deformations. The proposed modeling and optimization framework can be readily extended to such cases, including the use of hyper elastic material models when large deformations become relevant.

Despite these restrictions, the linear elastic approach remains valid as the investigated adhesion phenomena are primarily governed by the elastic response of the structure. Furthermore, the modular nature of this approach allows for such future extensions to account for non-homogeneous material distributions, material damage (e.g. Mullins effect), or environmental factors like temperature and humidity. By integrating advanced material models into the automated simulation pipeline, the neural network can be retrained to provide a more comprehensive tool for adhesive design.

Conclusions

In this study, a surrogate-based shape optimization framework was developed that couples automated finite element simulations with a narrow feedforward neural network to predict adhesion-relevant asymptotic stress parameters. It was demonstrated that the relationship between spline-based punch geometry and the corresponding asymptotic stress characteristics can be captured with high accuracy using a neural network with a small number of trainable parameters, achieving reliable predictive performance without relying on deep or overparameterized neural network architectures.

For spline-defined punch geometries characterized by four control points, the framework enables the identification of an optimal shape that minimizes the asymptotic normal stress in the edge singularity domain under purely normal loading conditions. The optimized spline-based punches achieve a reduction of the asymptotic stress distribution by approximately 25.5% compared to the straight punch benchmark, indicating a substantial improvement in the attainable adhesion performance. This optimization is made possible by the significant computational efficiency of the surrogate model, which provides a speed-up factor of more than 3×10^5 compared to traditional finite element analysis. While direct simulations would require over 41 h for 10, 000 configurations, the neural network completes the same task in less than half a second. This performance gain enables a comprehensive exploration of the spline-based design space. Beyond the identification of optimal shapes, this approach provides quantitative insight into how local geometric variations influence the asymptotic stress solution in the vicinity of the contact edge.

The study further introduced a fully automated finite element workflow implemented using Abaqus and Python scripting, allowing for large-scale parametric investigations and reproducible dataset generation with minimal manual intervention. All simulation data, regression results, and trained surrogate models are stored in structured and reusable formats, ensuring reproducibility and enabling the framework to be applied to other adhesion-related geometry optimization problems. Owing to its modular design, the proposed methodology can be extended to account for non-homogeneous material distributions, composite pillar architectures, alternative loading conditions, or more advanced interfacial models.

Furthermore, the results demonstrate that the punch perimeter geometry directly influences the slope of the asymptotic stress solution, β. By modifying the local tangent angle, the nature of the stress singularity is altered relative to the reference straight cylindrical punch. A more comprehensive analytical investigation into the relationship between the spline-based tangent angle and the singularity exponent remains a subject for future research.

ORCID iD

Attila Kossa https://orcid.org/0000-0003-3638-3237

Funding

The authors disclosed receipt of the following financial support for the research, authorship, and/or publication of this article: This research was supported by the Hungarian National Research, Development and Innovation Fund of the Ministry of Culture and Innovation, under project no. FK 142457. The scientific results presented in this study were achieved with the support of the János Bolyai Research Scholarship of the Hungarian Academy of Sciences. The project supported by the Doctoral Excellence Scholarship Program (DKÖP) was implemented with the support of the Hungarian National Research, Development and Innovation Fund of the Ministry of Culture and Innovation, as well as the Budapest University of Technology and Economics.

Declaration of conflicting interests

The authors declared no potential conflicts of interest with respect to the research, authorship, and/or publication of this article.

Supplemental material

Supplemental material for this article is available online. The data and the code will be made available on the corresponding GitHub repository (https://github.com/nagocs).

References

1. Wang W, Liu Y and Xie Z. Gecko-like dry adhesive surfaces and their applications: a review. *J Bionic Eng* 2021; 18: 1011–1044. https://doi.org/10.1007/s42235-021-00088-7
2. Yu J, Chary S, Das S, et al. Gecko-inspired dry adhesive for robotic applications. *Adv Funct Mater* 2011; 21: 3010–3018. https://doi.org/10.1002/adfm.201100493
3. Glick P, Suresh SA, Ruffatto D, et al. A soft robotic gripper with gecko-inspired adhesive. *IEEE Robot Autom Lett* 2018; 3: 903–910. https://doi.org/10.1109/lra.2018.2792688
4. Ben-Larbi MK, Hensel R, Atzeni G, et al. Orbital debris removal using micropatterned dry adhesives: review and recent advances. *Prog Aerosp Sci* 2022; 134: 100850. https://doi.org/10.1016/j.paerosci.2022.100850
5. Hensel R, Moh K and Arzt E. Engineering micropatterned dry adhesives: from contact theory to handling applications. *Adv Funct Mater* 2018; 28: 1800865. https://doi.org/10.1002/adfm.201800865
6. Samri M, Thiemecke J, Prinz E, et al. Predicting the adhesion strength of micropatterned surfaces using supervised machine learning. *Mater Today* 2022; 53: 41–50. https://doi.org/10.1016/j.mattod.2022.01.018
7. Wang S, Fang Y, He H, et al. Wearable stretchable dry and self-adhesive strain sensors with conformal contact to skin for high-quality motion monitoring. *Adv Funct Mater* 2021; 31: 2007495. https://doi.org/10.1002/adfm.202007495
8. Zhang X, Wang Y, Tian Z, et al. A bioinspired snap-through meta structure for manipulating micro-objects. *Sci Adv* 2022; 8(46): eadd4768. https://doi.org/10.1126/sciadv.add4768
9. Arzt E, Quan H, McMeeking RM, et al. Functional surface microstructures inspired by nature – from adhesion and wetting principles to sustainable new devices. *Prog Mater Sci* 2021; 120: 100823. https://doi.org/10.1016/j.pmatsci.2021.100823
10. Spuskanyuk AV, McMeeking RM, Deshpande VS, et al. The effect of shape on the adhesion of fibrillar surfaces. *Acta Biomater* 2008; 4(6): 1669–1676. https://doi.org/10.1016/j.actbio.2008.05.026

11. Carbone G and Pierro E. A review of adhesion mechanisms of mushroom-shaped micro-structured adhesives. *Meccanica* 2013; 48: 1819–1833. https://doi.org/10.1007/s11012-013-9724-9
12. Afferrante L and Carbone G. The mechanisms of detachment of mushroom-shaped micro-pillars: from defect propagation to membrane peeling. *Macromol React Eng* 2013; 7(11): 609–615. https://doi.org/10.1002/mren.201300125
13. Li Q, Wilhayn J, Lyashenko IA, et al. Adhesive contacts of rough elliptical punches. *Mech Res Commun* 2022; 122: 103880. https://doi.org/10.1016/j.mechrescom.2022.103880
14. Gorb S, Varenberg M, Peressadko A, et al. Biomimetic mushroom-shaped fibrillar adhesive microstructure. *J R Soc Interface* 2007; 4: 271–275. https://doi.org/10.1098/rsif.2006.0164
15. Carbone G, Pierro E and Gorb SN. Origin of the superior adhesive performance of mushroom-shaped micro-structured surfaces. *Soft Matter* 2011; 7: 5545–5552. https://doi.org/10.1039/c0sm01482f
16. Zhang X, Wang Y, Hensel R, et al. A design strategy for mushroom-shaped microfibrils with optimized dry adhesion: experiments and finite element analyses. *J Appl Mech* 2021; 88: 1. https://doi.org/10.1115/1.4049183
17. Betegón C, Rodríguez C, Martínez-Pañeda E, et al. Pull-off strength of mushroom-shaped fibrils adhered to rigid substrates. *arxiv 2506.20745*. 2025. https://arxiv.org/abs/2506.20745
18. Li D, Yan Y, Li R, et al. Insight into the dynamic adhesion of bio-inspired mushroom-shaped micropillars. *Tribol Int* 2026; 214: 111274. https://doi.org/10.1016/j.triboint.2025.111274
19. Aksak B, Sahin K and Sitti M. The optimal shape of elastomer mushroom-like fibers for high and robust adhesion. *Beilstein J Nanotechnol* 2014; 5: 630–638. https://doi.org/10.3762/bjnano.5.74
20. Kossa A, Hensel R and McMeeking RM. Adhesion of a cylindrical punch with elastic properties that vary radially. *Mech Res Commun* 2023; 130: 104123. https://doi.org/10.1016/j.mechrescom.2023.104123
21. Balijepalli RG, Fischer SCL, Hensel R, et al. Numerical study of adhesion enhancement by composite fibrils with soft tip layers. *J Mech Phys Solids* 2017; 99: 357–378. https://doi.org/10.1016/j.jmps.2016.11.017
22. Chen SW, Wang GF and Ciavarella M. Optimal grading of elastic modulus at contact corners with friction with application in fibrillar adhesives. *European JMech- A/Solids* 2025; 113: 105673. https://doi.org/10.1016/j.euromechsol.2025.105673
23. Riddoch DJ and Hills DA. Necessary conditions for near-edge stick of complete contacts. *J Strain Anal Eng Des* 2020; 55(5-6): 172–180. https://doi.org/10.1177/0309324720902873
24. Hills DA, Dini D, Magadu A, et al. A review of asymptotic procedures in stress analysis: known solutions and their applications. *J Strain Anal Eng Des* 2004; 39(6): 553–568. https://doi.org/10.1243/0309324042379275
25. Khaderi SN, Fleck NA, Arzt E, et al. Detachment of an adhered micropillar from a dissimilar substrate. *J Mech Phys Solids* 2015; 75: 159–183. https://doi.org/10.1016/j.jmps.2014.11.004
26. Balijepalli RG, Begley MR, Fleck NA, et al. Numerical simulation of the edge stress singularity and the adhesion strength for compliant mushroom fibrils adhered to rigid substrates. *Int J Solids Struct* 2016; 85-86: 160–171. https://doi.org/10.1016/j.ijsolstr.2016.02.018
27. Carpinteri A and Paggi M. On the asymptotic stress field in angularly nonhomogeneous materials. *Int J Fract* 2005; 135(1-4): 267–283.
28. Horváth AL and Kossa A. Stability maps for the slightly compressible poker chip detachment problem. *Finite Elem Anal Des* 2024; 242: 104257. https://doi.org/10.1016/j.finel.2024.104257
29. Li R, Li D, Sun J, et al. Pull-off dynamics of mushroom-shaped adhesive structures. *J Mech Phys Solids* 2024; 183: 105519. https://doi.org/10.1016/j.jmps.2023.105519
30. Kim Y, Yang C, Kim Y, et al. Designing an adhesive pillar shape with deep learning-based optimization. *ACS Appl Mater Interfaces* 2020; 12: 24458–24465. https://doi.org/10.1021/acsami.0c04123
31. Kim Y, Yeo J, Park K, et al. Designing directional adhesive pillars using deep learning-based optimization, 3D printing, and testing. *Mech Mater* 2023; 185: 104778. https://doi.org/10.1016/j.mechmat.2023.104778
32. Son D, Liimatainen V and Sitti M. Machine learning-based and experimentally validated optimal adhesive fibril designs. *Small* 2021; 17: 2102867. https://doi.org/10.1002/smll.202102867
33. Pande SS and Turner KT. Geometric optimization of pillars for enhanced adhesion. *Extrem Mech Lett* 2023; 59: 101969. https://doi.org/10.1016/j.eml.2023.101969
34. Luo A, Zhang H and Turner KT. Machine learning-based optimization of the design of composite pillars for dry adhesives. *Extrem Mech Lett* 2022; 54: 101695. https://doi.org/10.1016/j.eml.2022.101695
35. Shojaeifard M, Ferraresso M, Lucantonio A, et al. Machine learning based optimal design of fibrillar adhesives. *arxiv 2409.25928*. 2024. https://arxiv.org/abs/2409.05928
36. Yu J and Ryu S. Deep reinforcement learning-based optimization for the shape of an adhesive pillar with enhanced adhesion strength. *J Mech Des* 2025; 147(9): 091703. https://doi.org/10.1115/1.4068747
37. Teixeira I, Castro I, Carvalho V, et al. Polydimethylsiloxane mechanical properties: a systematic review. *AIMS Mater Sci* 2021; 8(6): 952–973.
38. Samri M, Kossa A and Hensel R. Effect of subsurface microstructures on adhesion of highly confined elastic films. *J Appl Mech* 2021; 88(3): 031009. https://doi.org/10.1115/1.4049182
39. Schneider F, Fellner T, Wilde J, et al. Mechanical properties of silicones for mems. *J Micromech Microeng* 2008; 18: 6. https://doi.org/10.1088/0960-1317/18/6/065008
40. Chollet F. Keras. 2015. https://keras.io/getting_started/faq/#how-should-i-cite-keras
41. Hunter JD. Matplotlib: a 2D graphics environment. *Comput Sci Eng* 2007; 9(3): 90–95. https://doi.org/10.1109/MCSE.2007.55
42. Harris CR, Millman KJ, van der Walt SJ, et al. Array programming with NumPy. *Nature* 2020; 585: 357–362. https://doi.org/10.1038/s41586-020-2649-2
43. Dassault Systèmes Simulia Corp. Abaqus/standard user's manual, version 2020. 2022.
44. Brunton SL and Kutz JN. *Data-driven science and engineering: machine learning, dynamical systems, and control*. Cambridge University Press, 2022.
45. Goodfellow I, Bengio Y and Courville A. *Deep learning*. MIT Press, 2016. http://www.deeplearningbook.org

46. Emmert-Streib F, Yang Z, Feng H, et al. An introductory review of deep learning for prediction models with big data. *Front Artif Intell* 2020; 3: 4.
47. Hornik K, Stinchcombe M and White H. Multilayer feedforward networks are universal approximators. *Neural Netw* 1989; 2(5): 359–366. https://doi.org/10.1016/0893-6080(89)90020-8
48. Hastie T, Tibshirani R and Friedman J. *The elements of statistical learning: data mining, inference, and prediction. Springer series in statistics*. Springer, 2009.
49. Bishop C. *Pattern recognition and machine learning. Information science and statistics*. Springer, 2016.
50. Keskar NS, Mudigere D, Nocedal J, et al. On large-batch training for deep learning: generalization gap and sharp minima. *arxiv 1609.04836*. 2017. https://arxiv.org/abs/1609.04836
51. Prechelt L. Early stopping - but when? In: Orr GB and Müller KR (eds) Neural Networks: Tricks of the Trade, Berlin, Heidelberg: Springer Berlin Heidelberg, 1998, pp. 55–69.
52. Storn R and Price K. Differential evolution – a simple and efficient heuristic for global optimization over continuous spaces. *J Glob Optim* 1997; 11: 341–359. https://doi.org/10.1023/A:1008202821328
53. Virtanen P, Gommers R, Oliphant TE, et al. SciPy 1.0: fundamental algorithms for scientific computing in python. *Nat Methods* 2020; 17: 261–272. https://doi.org/10.1038/s41592-019-0686-2
54. Violano G, Dibitonto S and Afferrante L. Role of viscoelasticity in the adhesion of mushroom-shaped pillars. *Bioinspir Biomim* 2024; 19(6): 066006. https://doi.org/10.1088/1748-3190/ad839d
55. Ji RG, Yuan YY, Liu XF, et al. Modeling the pull-off force of a mushroom-shaped fibrillar adhesive in dynamic detachment. *Int J Solids Struct* 2025; 308: 113150. https://doi.org/10.1016/j.ijsolstr.2024.113150
56. Horváth AL and Kossa A. Detachment stability maps of bi-material composite fibrils. *Mech Res Commun* 2025; 150: 104555. https://doi.org/10.1016/j.mechrescom.2025.104555

Appendix 1

Dataset structure

This appendix describes the structure of the dataset generated by the automated finite element simulations and subsequently postprocessed using Python. The dataset is provided in two complementary formats: a `CSV` file (Listing 1) summarizing the key parameters for each punch configuration, and a `JSON` (Listing 2) file containing detailed metadata together with the complete interfacial stress distribution and its asymptotic approximation. This format provides a simple way to store heterogeneous data in single file.

Each row of the `CSV` file corresponds to a single simulation that successfully converged. The recorded columns include the geometric design variables, the spline tangent angle φ, the asymptotic stress regression parameters (α, β), and the coefficient of determination R^2 characterizing the quality of the asymptotic fit. This file is used for training the neural network model.

Listing 1: Example entry of the CSV dataset

```
C2_r,C2_z,C3_r,C3_z,phi,beta,alpha,R2
0.78,1.25,0.52,0.5,33.94,0.249,-0.431,0.999
```

The `JSON` files store the complete output of the finite element simulations together with the results of the regression analysis for each individual configuration. In addition to the geometric metadata ($C2_r$, $C2_z$, $C3_r$, $C3_z$, φ), the files contain the asymptotic regression parameters α and β, the R^2, the full interfacial normal stress distribution $\sigma(\rho)$, and its asymptotic counterpart $\sigma_\infty(\rho)$.

Listing 2: Example of a JSON dataset

```
{
  ''metadata'':{
       ''C2_r'': 0.783,
       ''C2_z'': 1.250,
       ''C3_r'': 0.525,
       ''C3_z'': 0.500,
       ''phi'': 33.94,
       ''beta'': 0.2495,
       ''alpha'': -0.4315,
       ''R2: 0.9996
    },
  ''sigma·z'':{
     ''rho'': [...],
     ''sigma_z'': [...]
    },
  ''sigma_inf'':{
     ''rho'': [...],
     ''sigma_z'': [...]
    }
}
```

The arrays rho and sigma_z contain between 120 and 150 entries, refined in the vicinity of the stress singularity.

Appendix 2

Influence of the Poisson's ratio

The influence of the Poisson's ratio on the stress distribution in fibrillar structures is discussed in several previous studies.[28,38,56] In the present work, a value of $\nu = 0.495$ was adopted to represent the typical behavior of PDMS material.[38] To evaluate the sensitivity of the results to this material parameter, additional finite element simulations were performed for two additional values of ν within the nearly incompressible range, including the incompressible limit ($\nu = 0.5$).

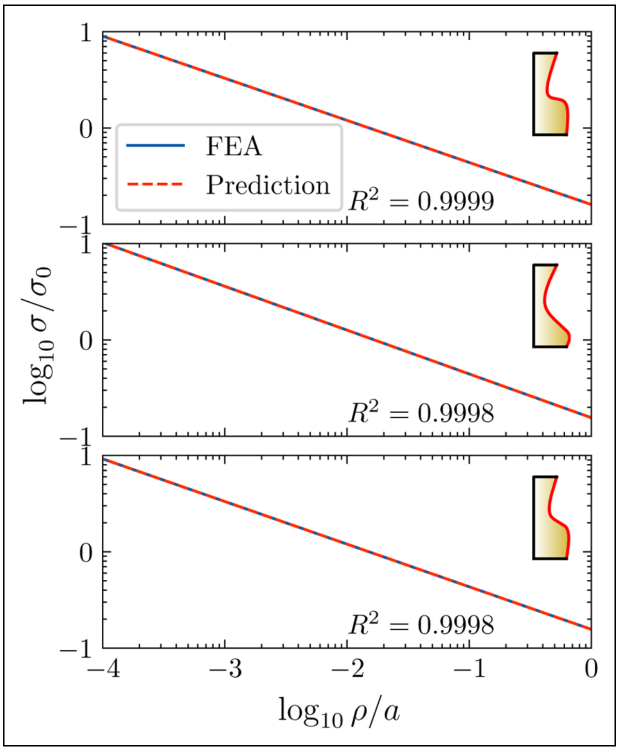

Figure 15. Comparison of the stress distribution obtained from finite element simulations for different values of the Poisson's ratio: $\nu = 0.495$ (red), $\nu = 0.5$ (blue), and $\nu = 0.49$ (green).
The differences are within the displayed line thickness, confirming the high degree of correlation (with $R^2 \geqslant 0.9998$).

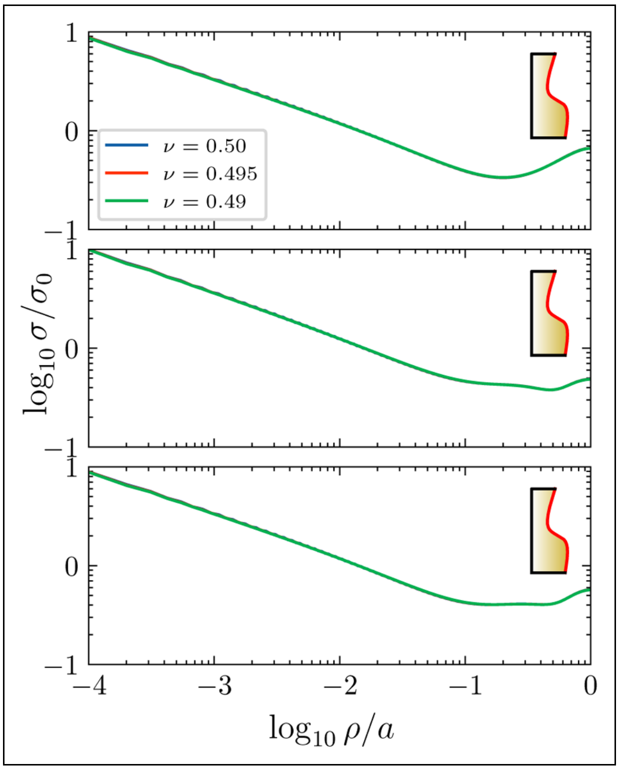

Figure 16. Comparison of the asymptotic stress solution for the optimized punch geometries obtained from finite element simulations and the neural network predictions.
The shown cases are referred later as #1, #2, and #3, corresponding to the three optimized geometries with the best performance.

The graphical comparison presented in Appendix Figure 15 shows the stress distributions obtained for the considered values of ν. A numerical comparison indicates that the stress solutions have a mean relative difference of 0.42% with respect to the reference case $\nu = 0.495$. The Poisson's ratio typically has a more significant influence in cases where material deformation is highly constrained, such as in thin films (poker chip geometry) or composite fibrils, as demonstrated in the literature.[28,56] In the present study, the investigated punch geometry does not represent such a critical configuration, resulting in the observed low sensitivity.

Note that this analysis was carried out using only direct finite element simulations. The neural network was trained using a fixed value of the Poisson's ratio, and therefore the surrogate model in its present form is not intended to predict the effect of varying material parameters.

Appendix 3

Validation of the prediction for the optimized punch geometry

This appendix presents a validation of the neural network predictions for the optimized punch geometries using direct finite element simulations. The aim of this comparison is to verify that the asymptotic stress solution predicted by the neural network is consistent with the solution obtained from finite element analyses for the optimized geometries. The validation is performed for the three best-performing optimized punch geometries identified through the surrogate-based optimization process, which correspond to the lowest predicted values of the dimensionless parameter C.

Table 6. Numerical comparison between the finite element simulations and the neural network predictions for the three investigated optimized geometries.

Parameter	#1	#2	#3
α_{FEA}	−0.8102	−0.7956	−0.8213
α_{pred}	−0.8215	−0.8104	−0.8129
$\varepsilon_{\text{rel},\alpha}$	1.4%	1.86%	1.02%
β_{FEA}	−0.4543	−0.4371	−0.4612
β_{pred}	−0.4591	−0.4444	−0.4587
$\varepsilon_{\text{rel},\beta}$	1.07%	1.65%	0.54%
C_{FEA}	0.2121	0.2168	0.2077
C_{pred}	0.2073	0.2105	0.2114
$\varepsilon_{\text{rel},C}$	2.24%	2.87%	1.77%

The subscripts "FEA" and "pred" denote the values obtained from the finite element analysis and the neural network surrogate model, respectively.

As shown in Appendix Figure 16, the asymptotic stress solution predicted by the neural network shows good agreement with the asymptotic stress solution obtained from the direct finite element simulations. The differences between the results obtained from the two computational methods are within the displayed line thickness. The corresponding R^2 values are indicated, reaching a minimum of 0.9998, which confirms the high degree of correlation.

A quantitative comparison between the finite element validation simulations and the predicted parameters is provided in Appendix Table 6. The results indicate that the relative deviation between the neural network predictions and the finite element results remains below 2% for the parameters α and β in all examined cases. The relative error associated with the parameter C is slightly higher, which can be attributed to the accumulation of numerical errors. Nevertheless, the deviation remains within the range of approximately 2%–3%.

These results indicate that the trained neural network is capable of predicting the asymptotic stress solution with good accuracy also for the optimized punch geometries within the investigated parameter range.